Journal of Colloid and Interface Science 682 (2025) 413–422

Contents lists available at ScienceDirect

Journal of Colloid And Interface Science

journal homepage: www.elsevier.com/locate/jcis

Regular Article

Wetting behavior in the inertial phase of droplet impacts onto sub-millimeter microstructured surfaces

Patrick Palmetshofer [a,*], Jonathan Wurst [a], Anne K. Geppert [a], Kathrin Schulte [a], Gianpietro Elvio Cossali [b], Bernhard Weigand [a]

[a] *Institute of Aerospace Thermodynamics, University of Stuttgart, Pfaffenwaldring 31, Stuttgart, 70569, Germany*
[b] *University of Bergamo, Via Einstein, Dalmine, 24044, Italy*

GRAPHICAL ABSTRACT

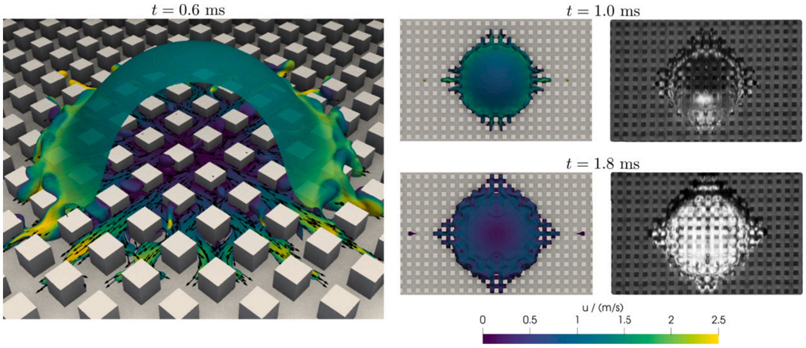

ARTICLE INFO

Dataset link: https://doi.org/10.18419/darus-4178

Keywords:
Wetting
Droplet impact
Surface structures
Imbibition
DNS

ABSTRACT

Hypothesis: The shape of the wetted region after a droplet impact can vary significantly even in the early phase of the process. How much of the early spreading process occurs within the structures versus above the structures, flow regimes and local wetting at groove intersections can have effects on the sizes and shapes of the final wetted regions.

Experiments and simulations: We experimentally study droplet impacts onto cubic pillars with 0.1 mm, 0.2 mm and 0.5 mm side length, height and separation. Weber numbers ranged between 80 and 1 100, while Reynolds numbers varied between 1 150 and 10 600 using water and isopropanol droplets. The contact angle on a flat segment of the samples was modified between $\theta_{FS} < 5°$ and $\theta_{FS} = 120° \pm 5°$. Several experiments are reproduced using our in-house code FS3D to show the internal flow fields.

Findings: Diamond-shaped spreading patterns with edges aligned at 45° to the structure pattern are observed. A transition between top-dominated (circular) spreading and diamond spreading occurs depending on the structure size and impact velocity. Groove intersections can act as flow dividers, causing spreading along a path with 90° bends. For large structure sizes and impact velocities fluid jets can pass through the structures uninhibited.

---

* Corresponding author.
E-mail address: patrick.palmetshofer@itlr.uni-stuttgart.de (P. Palmetshofer).

https://doi.org/10.1016/j.jcis.2024.11.154
Received 3 September 2024; Received in revised form 12 November 2024; Accepted 20 November 2024

1. Introduction

The continuous improvements of manufacturing techniques allow substrate surfaces to be designed very specifically for a particular purpose. Processes where drop impact is prevalent are very suitable for such surface modifications and include regularly structured surfaces. A better understanding of how imbibition into structured surfaces occurs during all phases of a droplet impact can lead to efficiency improvements in various applications such as spray cooling [1–3] or in new technologies like self-cleaning surfaces [4,5]. Thus, numerous studies have investigated the capillary imbibition dynamics into structured surfaces [6–8], but the differences in dynamic wetting if higher-velocity flow passes through the surfaces have mostly been treated separately from the capillary spreading. However, such a fast-flowing phase of the wetting process can dominate the final state of the wetted area, as previously shown for droplet impacts by Sivakumar et al. [9]. Also, studies on droplet impacts onto structured surfaces have often either focused on structure sizes similar to the droplet size [10,11] or much smaller than it [12,13]. In many of these cases, hydrophobic surfaces were a focus of the study [14–16], as the potential of microstructures in creating superhydrophobic surfaces has been explored [17,18]. Relatively few studies, however, have investigated regular structures in the sizes which are approximately one order of magnitude smaller than the droplet and how the dynamics of the impact process can affect the wetting and later capillary imbibition on the surfaces. Similar relative structure sizes can, for example, be found in micrometric droplet impacts onto micrometric surface structures or impacts of large droplets onto structures aimed at increasing heat transfer rates for spray cooling. Hydrophilic surfaces [19–21] were also reported more seldom than hydrophobic surfaces [16,22]. In the cases with hydrophilic surfaces, the final spreading shape was often dominated by capillary spreading [23,24] and the early behavior of the droplet impact was similar to impacts on smooth surfaces.

For droplet diameters in the same order of magnitude as the capillary length of water under ambient conditions, 2.7 mm, the intermediate size range corresponds to structures on the order of hundreds of micrometers. Notable experimental studies in this size range using water droplets were reported by Vaikuntanathan et al. [25], who used grooved surfaces and Sivakumar et al. [9], who used cuboid pillars with pillar heights between 0.1 mm and 0.5 mm, a very similar configuration to ours, with a fixed width and separation of 0.3 mm. In their study, Sivakumar et al. reported two separate but simultaneous flow regions: one above the pillars and one in the grooves between the pillars. They observed that while the bottom (groove) spreading propagates at a similar rate as on a flat surface, the top spreading velocity is lower, leading to much larger spreading factors for liquid in the grooves compared with only considering liquid above the pillars. They also observed how liquid jets can develop in the grooves between the structure elements. For the final state, they report a rhombus (diamond) spreading shape. For higher Weber numbers their reported spreading shapes can feature additional protrusions along the grooves which cross close to the initial impact point. They explain this by the variation of the velocity component along the groove for each impact.

Tan [26] numerically reproduced some of the results of Sivakumar et al. [9] in the validation of their numerical code and was able to reproduce the diamond shape. In their study on micrometric droplets impacting onto micrometrically structured surfaces, they also report varying spreading shapes for different pillar separation, in some cases reaching diamond-like shapes as well. While Sivakumar et al. [9] show experimentally that these shapes are formed, Tan [26] provides numerical simulations for the same. However, a detailed explanation for the development of the different shapes formed during spreading remains elusive.

In a general sense, we aim to provide a comprehensive picture in the understanding of dynamic wetting of regularly structured surfaces. For this, as reported in the following section 2, we investigate droplet impacts onto surfaces with cubic structure elements between 0.1 mm and 0.5 mm in size and separation, by investigating both water and isopropanol droplets falling onto the surfaces. Notably, to record the wetting process, our use of a total internal reflection (TIR) for the bottom view provides accurate tracking of the contact line. Additionally, by using our in-house numerical code Free Surface 3D (FS3D) [27] on a high performance computer, we are able to explain the phenomena which lead to the formation of the diamond shapes in detail. This allows insights into the microscopic flow dynamics in the grooves between and above the pillars.

Through this, we explain how the wetted structured surface in the early phase of a droplet impact [16] can depend on the impact parameters for a variety of cases. For this, we focus how spreading occurs inside or above the structures, as discussed in section 3.1, how jets or meandering flow can develop in the structures (section 3.2) and how the structure geometry affects the spreading factors. We further use both simulations and experiments to discuss the mechanisms that cause diamond-shaped wetted regions, as reported in section 3.3.

Table 1
Contact angles of the used fluids on flat fused silica samples for different treatments. Contact angle measurements on flat surfaces were repeated for every measurement day.

Surface treatment	Water	Isopropanol
Activated	$< 5°$	-
None	$40° < \theta_{FS} < 55°$	$< 5°$
Polymerized	$120° \pm 5°$	$70° \pm 5°$

2. Materials and methods

To study the effect of surface structures on droplet wetting in early impact phases, we used transparent surface samples made from fused silica. High-speed imaging was used in conjunction with image data processing in MATLAB to determine the impact velocity and droplet diameter as well as the diagonal and axial spreading factors. The experiments were supported by direct numerical simulations using the experimentally recorded impact parameters as initial conditions.

2.1. Investigated surfaces and treatment

The fused silica surfaces were manufactured by *LightFab GmbH Germany* using selective laser-induced etching [28]. Three types of surfaces were used, all featuring cubic pillars on a square lattice. The size d_s of the pillars was 0.1 mm, 0.2 mm, and 0.5 mm, for the smallest, intermediate and largest structure sizes, respectively. Due to the manufacturing process, the edges, both at the top and bottom of the pillars could be made sharp, with edge radii $< 1\,\mu\text{m}$ while the horizontal variation of the depth of the grooves was $< 5\,\mu\text{m}$. The pillar size d_s here refers to the side length, height and separation of the pillars, corresponding to a pitch (distance between repeating elements) of $2d_s$.

Similarly to the work of Foltyn et al. [24], we modified the inherent surface wettability (and thus the contact angle on the flat material θ_{FS}) by plasma polymerization, performed using a *Diener electronic Femto* plasma machine to increase the contact angle and plasma activation with a similar *Diener electronic Femto SLS* machine to decrease the contact angle. We verified the contact angle range by gently placing a sessile droplet on the flat section of the surface sample and using a *DataPhysics OCA 15EC* contact angle measurement device. The resulting contact angles are summarized in Table 1. As the ranges given include measurements of the static, advancing and receding contact angles, the rough ranges given in Table 1 should also include Young's contact angle for each given treatment [29].

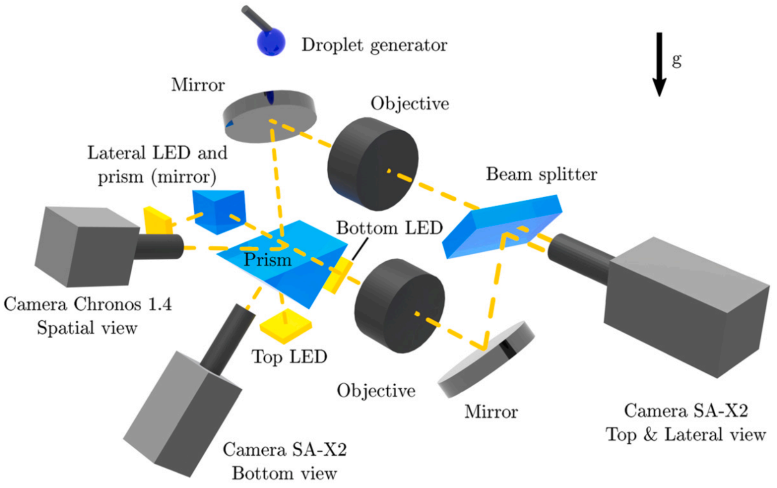

Fig. 1. Schematic of the experimental setup (not to scale). Holders, focusing optics for the LEDs and shading near the beam splitter to separate the top and lateral view are not displayed.

Table 2
Fluid properties of water and isopropanol at 25 °C.

Property	Unit	Water	Isopropanol	Ref.
Surface tension γ_{LG}	$\mathrm{mN\,m^{-1}}$	72.0	20.9	[31,32]
Dynamic viscosity μ	mPa s	0.890	2.04	[33,34]
Density ρ	$\mathrm{kg/m^3}$	997	782	[35,36]

2.2. Experimental methods

To study the droplet impacts, we used the multi-perspective test stand displayed in Fig. 1, which was originally developed and described by Foltyn [30]. The test stand can record the spreading process from four perspectives simultaneously. In the setup, the top and lateral views are combined onto a single sensor of a *Photron SA-X2* high speed camera using an intermediate image near a beam splitter plate. The bottom view is recorded using the same camera model and both cameras are synchronized at a frame rate of 20 000 fps and a shutter speed of 11 µs. A third camera (Krontech Chronos 1.4) is used to record the impact from a fourth “spatial” perspective at a 90° angle with respect to the side view and at an inclination of approximately 20°. The bottom view is configured as a total internal reflection (TIR) perspective, meaning that the droplet is not visible on the camera before it reaches the surface. This also enables accurate tracking of the contact line in the grooves as the contact line appears as a dark line. Both deionized water (DIN 43530) and isopropanol (Chemsolute > 99.9%) were dropped from a blunt needle (*Braun Sterican 27G*) with an outer diameter of 0.4 mm, connected to a medical syringe pump (*KD Scientific Legato 210*) through flexible PTFE tubing. The fluid properties are given in Table 2. For falling heights of 0.7 m and 1.2 m a cardboard tube was placed around the falling path to ensure a consistent impact position. A single droplet was chosen out of a continuous chain of detaching droplets by removing a glass beaker or paper in the path for a short duration.

2.3. Image processing and analysis

A checkerboard calibration pattern was used to determine the distortion, scale and offset of all four perspectives. The bottom, top and lateral perspectives were used to automatically determine impact and spreading parameters using a MATLAB program. After a background subtraction and cleaning procedure, the images were binarized. The last 10 frames before impact were used to determine the droplet diameter and velocity from the lateral view. As the droplet can be somewhat oblate due to aerodynamic forces during the falling process, the diameter determination $D_0 = \sqrt{4A/\pi}$ was performed using an average projected area A determined from the images [37]. The bottom view was used to track the contact line and continuous wetted area in the grooves. In a post-processing step, the maximum extent of a continuously wetted area in the axial directions along the pillar orientation and both diagonal directions at 45° to the former were determined by using the difference of the maximum radii from the impact point in a 10° wedge.

2.4. Numerical methods

The simulations in this study are conducted with our in-house incompressible multiphase flow solver Free Surface 3D (FS3D) [27]. It employs the finite volume method on a Cartesian staggered grid. The Volume-of-Fluid (VoF) method [38], together with the piecewise linear interface calculation [39] (PLIC) tracks the phase distributions. The surface tension forces are determined based on Lafaurie [40]’s continuum surface stress (CSS) model with modifications by Steigerwald et al. [41]. The CSS model was shown to reproduce other high-speed applications like drop-drop collisions [42] or drop-film impacts [41] and especially handles large morphological changes like jetting well. The dynamic contact angle is calculated using Mathieu’s [43] approximation of Cox’s theory [44]. A sketch of the numerical setup is shown in Fig. 2. All simulations were performed on a Cartesian equidistant grid with $512 \times 512 \times 512$ grid cells. A grid study revealed that further refinement of the grid results in no significant change of the flow features discussed in this paper. The grid study and further details on the numerical methods are presented in supplementary materials B.

2.5. Parameter space

The impact velocity was varied by changing the falling height of the droplet between 0.15 m and 1.2 m. Due to the different surface tensions and wetting properties of isopropanol and water with respect to the needle, water droplets had a mean projected area-averaged diameter of 2.2 mm while isopropanol droplets were 1.9 mm in size. As droplet impacts are commonly characterized by the Weber number We, relating inertia to surface tension forces, and the Reynolds number Re, relating inertia to viscous forces, these two parameters are used to discuss the differences between liquids and falling heights. The Weber number and Reynolds number are defined as

$$\mathrm{We} = \frac{\rho U_0^2 D_0}{\gamma_{LG}} \tag{1}$$

$$\mathrm{Re} = \frac{\rho U_0 D_0}{\mu} \tag{2}$$

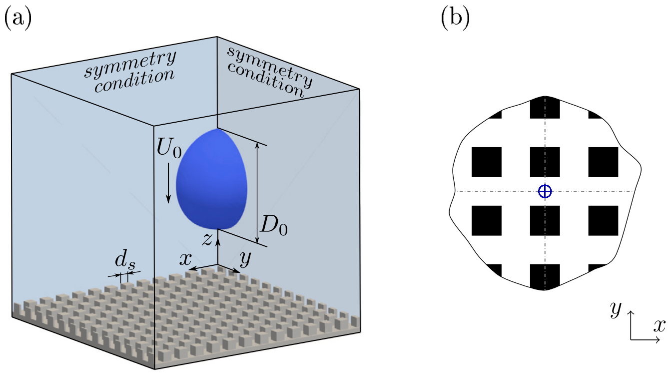

Fig. 2. Numerical setup. (a): Sketch of the computational domain with impact parameters and highlighted symmetry boundary conditions. (b): Impact position (marked as blue cross-circle) used in the numerical simulations. Black areas represent pillars, while grey lines show the symmetry axes which were used to reduce cell count. (For interpretation of the colors in the figure(s), the reader is referred to the web version of this article.)

Table 3
Reynolds and Weber numbers for the experimental parameters used in this study. Deviations represent standard deviation between determined impact parameters of 4 and 6 repetitions per parameter combination.

Water, droplet size: $D_0 = 2.2 \pm 0.1$ mm

Falling Height	0.15 m	0.3 m	0.7 m	1.2 m
U_0 / (m/s)	1.64 ± 0.01	2.29 ± 0.01	3.38 ± 0.03	4.22 ± 0.04
Re	4,040	5,400	8,670	10,600
We	80	150	350	560
Observed Regime	Deposition/ Part. Reb.	Deposition/ Splash	Splash	Splash

Isopropanol, droplet size: $D_0 = 1.9 \pm 0.1$ mm

Falling Height	0.15 m	0.3 m	0.7 m	1.2 m
U_0 / (m/s)	1.61 ± 0.01	2.24 ± 0.01	3.22 ± 0.03	3.99 ± 0.04
Re	1,150	1,600	2,300	2,900
We	180	350	730	1,100
Observed Regime	Deposition	Deposition/ Splash	Splash	Splash

where ρ is the density of the liquid, U_0 is the impact velocity, D_0 is the impact diameter, γ_{LG} is the surface tension (liquid-gas surface energy) and μ is the liquid dynamic viscosity. As shown in Table 3, the impact velocities ranged between $1.61\,\mathrm{m\,s^{-1}}$ and $4.22\,\mathrm{m\,s^{-1}}$, yielding impact Weber numbers from 80 to 1,100 and Reynolds numbers between 1,150 and 10,600.

For each falling height and structure size the wettability was varied as shown in Table 1 between a contact angle on the flat part of the surface of $< 5°$ and 120° for water and between $< 5°$ and 70° for isopropanol. All combinations of structure size, liquid, falling height and wettability result in a parameter space consisting of 48 different points, for each of which between 4 and 6 repetitions were performed. In the scope of this study, the cases using untreated surfaces for water droplets ($40° < \theta_{FS} < 55°$) and polymerized surfaces for isopropanol droplets ($\theta_{FS} \approx 70°$) are emphasized.

3. Results and discussion

To keep this paper brief, we will elaborate on how the wetted region forms due to flow inside or above the structures, jets in the structures and the resulting wetting shapes. We intentionally omit a discussion of some other phenomena in the droplet impact process, such as splashing [45], receding [46], rebound [47] and air entrapment [48]. In the following section, we show that the formation of a diamond-like spreading shape for intermediate wettabilities is dominated by the inertial spreading phase. The resulting final shapes range from near-circularly wetted regions for low structure sizes and impact velocities to sharp-tipped star-like regions at high impact velocity and structure sizes.

For hydrophilic surfaces, a distinction is possible between an inertial spreading phase and a capillary phase, where the spreading process is dominated by wettability.

In this work, we differentiate between the inertial phase of the spreading process on hydrophilic surfaces and the capillary phase using the non-dimensional inertial time τ_i

$$\tau_i = t\frac{U_0}{D_0} \tag{3}$$

where U_0 denotes the impact velocity, D_0 is the impact diameter and t is the physical time. We select $\tau_i = 2$ as the transition time. This is motivated by the fact that in many cases, the spreading dynamics for similar impact conditions on the same surface are observed to be relatively independent at early times after impact. Using this definition, some phenomena specific to the inertial phase can be discussed separately from capillary imbibition which can happen later in the process.

3.1. Wetting due to top or groove flow

In the inertial phase, our observations reveal that the spreading morphology seems to be strongly affected by whether the majority of the fluid which has reached the surface spreads above the pillars or in the channels between the pillars. Three types of flow can be differentiated as illustrated in Fig. 3a: Top-dominated flow, intermediate top-driven flow and groove-driven flow. Top-dominated flow predominantly occurs over the pillars and mostly happens for hydrophobic surfaces [49], where liquid penetration into the surface structures happens only very close to the impact point. Tan [26] reported this behavior on surfaces which are neither hydrophobic nor hydrophilic ($\theta_Y = 90°$) using numerical simulations, albeit at much lower Reynolds numbers than shown in this study. For impact cases which are predominantly top-dominated, a classical lamella-rim shape is formed. For our relatively large grooves and impact conditions, this mode is not observed as compared to many studies in literature, our structures and Weber numbers were relatively large.

Top-driven flow, the intermediate case is shown as an extract of a numerical simulation on the left side and center of Figs. 3a and 3b. Here, the fluid advances further in the grooves than on top of the pillars. However, the evolution of the droplet is still dominated by the higher portion of the fluid advancing on top of the pillars pushing the liquid between the pillars.

Lastly, in the groove-driven regime, most of the spreading occurs between the pillars far away from any driving flow over the pillar tops. The last numerical image shown in Fig. 3a is clearly groove-dominated. We find that whether top or groove spreading is dominant can depend on the size and separation of the pillars, the impact parameters and the wettability.

In the following, we show the influence of the structure and impact conditions on the aforementioned regimes. While from the experimental results only the flow above the pillars is visible, the numerical simulations allow us to also observe the flow in the grooves. The images in Fig. 3b show that which regime is dominant can depend on the time after impact. The evolution of spreading shape follows similar patterns initially, but deviations occur earlier in smaller structures, indicating scale-dependent variations. Very early after the initial impact ($\tau_i = 0.4$), the spreading behavior above the pillars appears groove-dominated for all structure sizes as long as the droplet resembles a cut sphere. However, already at $\tau_i = 1.5$, the maximum spreading diameter within the grooves is highest for the largest structure size compared with the smaller structures. For the 0.1 mm structures, spreading over the pillar tops reaches the same distance from the impact point as the groove spreading and now appears to drive the flow in the grooves.

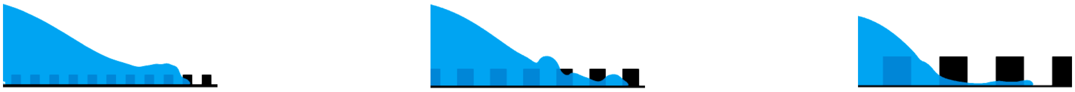

(a) Simulation snapshots emphasizing the extent of the wetted area in the grooves and over the tops of the pillars at $t = 1\,\mathrm{ms}$ ($\tau_i = 0.8$) for droplet impacts onto untreated samples with $d_s = 0.1\,\mathrm{mm}$ (left, top-driven), $d_s = 0.2\,\mathrm{mm}$ (center, top-driven), $d_s = 0.5\,\mathrm{mm}$ (right, groove-dominated) structure size.

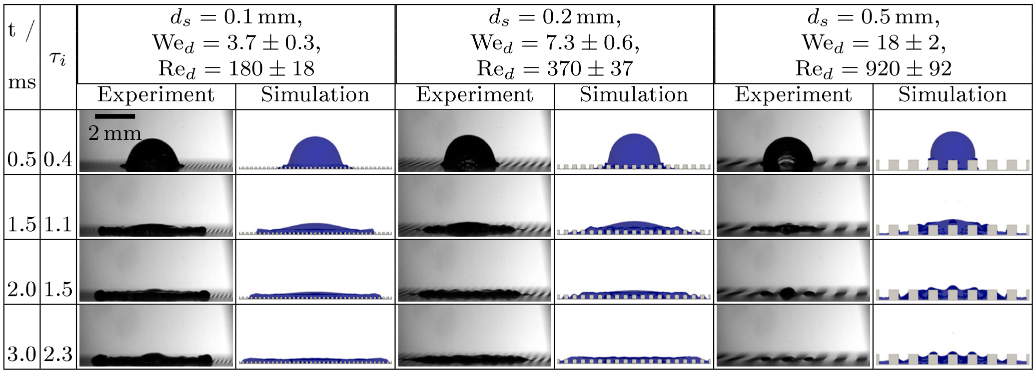

(b) Comparison of inertial imbibition behavior for water droplet impacts onto untreated samples (exp. $40^\circ < \theta_{FS} < 55^\circ$, sim. $\theta_Y = 50^\circ$) of different structure size for droplet impacts from 0.15 m ($\mathrm{We} = 80$, $\mathrm{Re} = 4040$)

Fig. 3. Explanation of top-driven spreading and groove-driven spreading (a) including example cases which cover the top-driven and groove-driven regimes (b).

Observing impact cases with another fluid or higher impact velocity reveals that larger groove sizes and higher impact velocities cause more groove spreading than top-dominated spreading. Thus, to characterize groove flow processes during the impact, we define structure specific Weber and Reynolds numbers,

$$\mathrm{We}_d = \frac{\rho U_0^2 d_s}{\gamma_{LG}} = \mathrm{We}\frac{d_s}{D_0} \tag{4}$$

$$\mathrm{Re}_d = \frac{\rho U_0 d_s}{\mu} = \mathrm{Re}\frac{d_s}{D_0} \tag{5}$$

which differ from the regular dimensionless parameters only in the choice of the reference length as the structure size d_s instead of the initial droplet diameter D_0. The resistance to fluid flow between the pillars is increased for higher viscosity or lower hydraulic diameters of the grooves corresponding to a lower Re_d. For the given impact cases, the structure-size specific Reynolds and Weber numbers are given in Fig. 3.

Even for the lowest Re_d case depicted in Fig. 3b, the impact appears to be dominated by inertia initially before viscosity has an effect by slowing down flow in the grooves. Due to viscosity, the boundary layer from the bottom of the grooves and the pillar sides grows into the grooves, decelerating the groove flow. This influences the spreading dynamics: the highest velocities of the advancing liquid-gas interface shift upwards within the grooves, similar to what is observed on smooth surfaces by Wildeman et al. [50]. Once this boundary layer reaches the top of the pillars at a distance smaller than a pillar length, the flow is fully top-driven. This means that, in terms of the classification of Fig. 3a, while groove flow is dominant for all cases at the earliest times, a transition to top-driven flow occurs at $\tau_i = 0.4$ for the 0.1 mm structures and starts at $\tau_i = 1.5$ for the 0.2 mm structures. For the 0.5 mm structures, the boundary layers do not reach the pillar tops before the final spreading shape is attained. As such, this case is fully groove-dominated.

The effect of the surface tension and contact angle, as long as it is in the hydrophilic range, appears to be relevant mostly for smaller structure sizes during lamella spreading over the pillar tops, as reported by Broom and Willmott [49]. In our hydrophilic cases, the bottom is usually wetted early in the impact process. At much later times than depicted in Fig. 3b when the initial impact inertia is mostly dissipated or converted into surface energy, capillary forces can dominate the flow. Here, the reader is referred to the work of Courbin et al. [8], who discussed imbibition phenomena into structured surfaces. Note that for hydrophobic surfaces, the surface energy difference is positive which can enhance top-dominated spreading as shown in the work of Broom and Willmott [49].

For more groove-driven flow, the lamella height over the pillars and radial extent is reduced when compared to top-driven flow, as more fluid is contained in the grooves. For the case with 0.5 mm structures, no lamella spreading is observed, indicating a case which is almost completely groove-dominated. In this case, wetting of the tops only occurs on pillars which are directly under the impacting droplet and (to some degree) above the neighboring grooves. In Fig. 3 at $\tau_i = 2.3$ (3 ms after the initial impact) no continuous volume of fluid over the surface is visible anymore, as most fluid has penetrated into the grooves. The only fluid on top of the pillars that remains at later times is on the three pillars which initially are directly underneath the falling drop. In fact, for all impacts on the 0.5 mm structures, we observe the formation of liquid caps under the impact point in all hydrophilic cases. As groove spreading plays an important role for many impact conditions investigated in this study, we aim to investigate it in more detail.

3.2. Spreading and jetting in groove-driven flow

For the locations and times in which groove-driven flow is dominant, a range of phenomena can be observed: when the fluid front reaches a groove intersection, the fluid can either form a jet following a single groove, which we subsequently call groove jetting, or the flow can split up at the intersection, as depicted in Fig. 4. In a first mode, a split-up of the flow happens if a liquid front reaches the edge of a pillar at an angle with respect to the grooves as seen in the upper portion of the $\theta_Y = 50^\circ$ case. Here, the edge of the pillar acts as a wedge, redirecting part of the fluid along one groove and another part along another, oriented orthogonally to the first. Depending on the incident angle different fractions of the flow are guided into each of the directions.

However, Fig. 4 illustrates that a split-up can also occur when parallel flow along a groove reaches an intersection as seen in the center of the $\theta_Y = 50^\circ$ case. When the flow in a groove is slow, the incident jet widens at each intersection. Both viscous friction at the groove bottoms, which decelerates the advancing liquid front and wetting of the hydrophilic groove bottoms can cause this widening. When reaching the

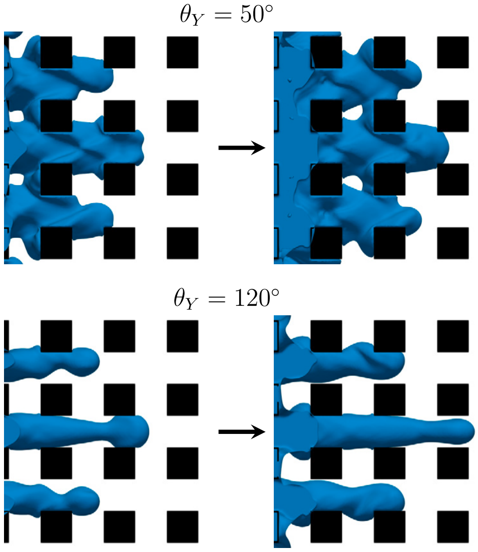

Fig. 4. Simulation snapshots for droplet impacts onto 0.2 mm structures for two different Young contact angles at the same impact conditions (Water, We = 80, Re = 1,150) illustrating flow-splitting at grooves or jetting along grooves.

next set of pillars with a footprint larger than the next groove, a part of the flow is thus redirected into the orthogonal groove.

When the contact line touches a new row of pillars, the wettability of the side surface determines whether an additional force acts inward (hydrophobic) or outward (hydrophilic) onto the contact line. Once an advancing contact line is established, the portion of the flow turning into the orthogonal groove increases. On the other hand, jetting which persists through intersections usually occurs when the liquid velocity in a groove is relatively high, leading to the formation of a pointed interface profile. Additionally, in cases with hydrophobic surfaces, groove jetting can occur at lower pore Reynolds numbers of the flowing liquid than on hydrophilic surfaces. This phenomenon is illustrated in Fig. 4, as both the central and off-center jets propagate along a single groove for the $\theta_Y = 120^\circ$ degree case, but groove-splitting (both orthogonal and wedge-splitting) occurs at lower contact angles. On hydrohobic surfaces and for very high impact Weber numbers, the advancing front of a jet is much thinner than the thickness of a groove and the jet can resemble the fingers in splashing on smooth surfaces. Such jets in the grooves can even lift off from the bottom of the grooves completely.

Similarly, Broom and Willmott [49] observed that at very early times, groove jetting can occur in the gaps between protrusions even on microstructures. These jets propagate exclusively axially along a groove. Note that jet spreading in the terminology of Sivakumar et al. [9] includes our groove jetting. Some of the jets they observed can persist throughout the full spreading process and dominate the final shape of the wetted region.

3.3. Development of the spreading shape

As mentioned in section 3.1, for low impact velocities, high viscosities and small structure sizes (low Re_d and We_d), the impact behavior can be similar to that on a microstructured or even smooth surface as a classical lamella-rim shape is formed above the pillars (top-dominated and top-driven cases). On the other hand, for very high impact velocities and all structure sizes, a jet-dominated spreading shape is formed, dominated by linear jets emanating from the impact area. In this section, we mainly discuss the intermediate range in which diamond-spreading occurs.

Fig. 5 shows the evolution of axial and diagonal spreading shapes at the end of the inertial phase and at $\tau_i > 50$ for water droplets hitting a $d_s = 0.1$ mm pillar structure surface from various falling heights. As previously discussed, most of the spreading process for the water droplet impacting onto the 0.1 mm surface displayed in Fig. 3b is driven by flow over the pillars. In Fig. 5a this corresponds to the case with a Weber number of We = 80. Two different spreading factors are differentiated in Fig. 5b: The diagonal spreading factor D_{45°/D_0 is illustrated by dashed lines and the axial spreading factor D_{0°/D_0 is indicated by solid lines, where axial and diagonal refer to the angle with respect to the orientation of the cubic surface structures. Comparing the curves in Fig. 5b, the circular lamella-spreading behavior for the lowest Weber number is confirmed, as the axial and diagonal spreading diameters develop similarly and remain on the same level throughout the observed spreading process. Fig. 5a also shows a clear lamella-rim shape at $\tau_i = 2$, confirming that this case is driven by flow over the pillar tops. This corresponds to a spreading factor ratio near 1.

For a Weber number of 153, a circle-like spreading shape, with a rim visible at $\tau_i = 2$ is still formed, albeit reaching a higher maximum spreading diameter and asymmetry. The spreading factor ratio remains slightly above unity.

At the two highest Weber numbers, the behavior is changed significantly: while the diagonal spreading factor stays similar to that in the We = 153 case, the axial spreading factor is strongly increased. The rim is no longer clearly distinguishable at $\tau_i = 2$ as the development of the spreading shape is dominated by flow in the grooves. Additionally, Fig. 5a shows dark spots at several locations in the final spreading shape, indicating air bubbles or dimples in the interface. The final spreading shape shifts towards the diamond spreading shape for higher impact velocities.

Note that in Fig. 5, the intermediate hydrophilic case is chosen, which is not affected by capillary spreading after $\tau_i \approx 5$ such that the final spreading shape and extent are dominated by the spreading in the inertial phase.

For the regimes where flow-splitting is dominant, once a splitting intersection is established as shown in Fig. 4, the difference in viscous flow resistance between axial and turning flow is low. Thus, each intersection acts as a divider for the flow, introducing a redirection pressure loss. Thus, the overall spreading length along the groove bottoms dominates the spreading shape. In this case, the spreading flow can be approximated as “taxicab spreading”, assuming that at each intersection the contact line either proceeds axially or turns by 90°. In this view, the spreading distance on the axis over the diagonal would be the taxicab (or Manhattan) distance, which is $D_{0^\circ}/D_{45^\circ} = \sqrt{2}$ times the axial spreading distance, resulting in the characteristic diamond (rhombus) shape. Fig. 6 illustrates this phenomenon.

This can be used as another classification parameter for the spreading process: for the spreading factor ratio at the end of the inertial phase $D_{0^\circ}/D_{45^\circ} = \sqrt{2}$ the flow was jet-spreading dominated, while for lower values it was dominated by a combination of taxicab spreading and/or top-driven spreading. In Supplementary Materials C, we give videos of the bottom view of four representative cases that illustrate circular spreading and flow-splitting spreading shapes.

Using numerical simulations, this behavior can be investigated in more detail. Fig. 7 shows a numerical simulation of an isopropanol droplet impact case onto a surface with superhydrophilic properties from the lowest investigated falling height (We = 180, Re = 1,160) from a top-down view and a 30° inclined view. At $\tau_i = 0.7$, the wedge splitting behavior at each intersection can be seen as well as jetting along the axial groove at the bottom. Later (See figure B.4 for $\tau_i = 1$), the jet thickness increases while the spreading rate decelerates due to viscous effects. At this instant, the rhomboidal spreading shape is already visible and it is fully developed at $\tau_i = 1.7$, as all last reached pillars are on a line diagonal to the grid orientation. Experimental images show the same behavior, with deviations between experiments and simulation remaining below one pillar size (< 0.2 mm, see figure B.4). Further evidence that this spreading shape is dominated by taxicab spreading can be gathered from pathlines determined from the simulations. Using the 2D-projected velocity field in the liquid in a plane half the height of the pillars, they show that the flow reaching the advancing contact

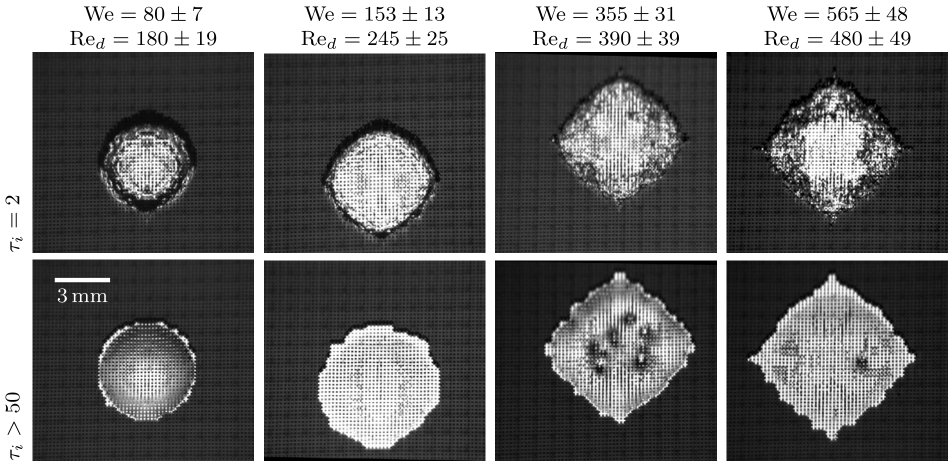

(a) Bottom view at the end of the inertial phase (top) and final view (bottom)

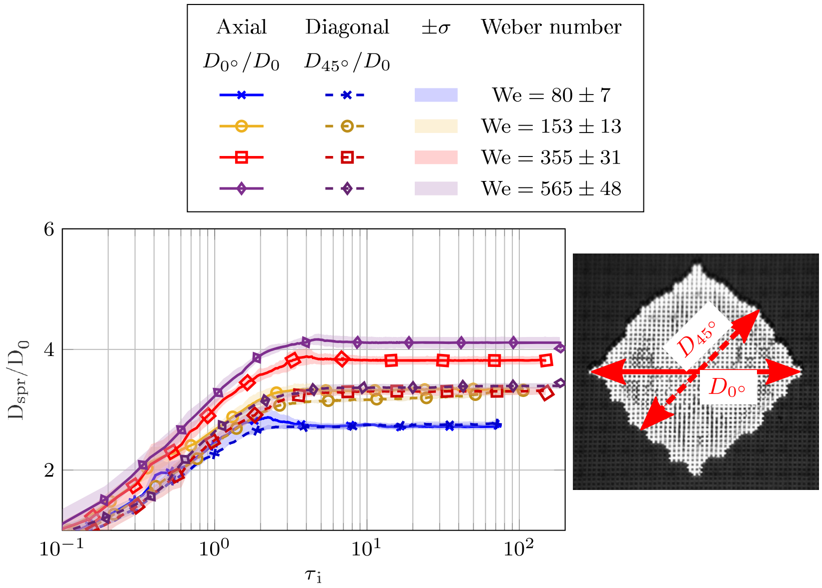

(b) Spreading factors D_{spr}/D_0 (axial $D_{0°}/D_0$ and diagonal $D_{45°}/D_0$) over time. Higher axial spreading at high Weber numbers, diagonal spreading only increased until threshold impact Weber number. Shaded regions represent standard deviation between 4-6 repetitions and two orthogonal axes (8-12 data points) for each parameter combination.

Fig. 5. Bottom view of spreading shapes (a), spreading factors (b) and their ratios (c) over time. Water droplet impacts from different falling heights onto untreated surfaces $40° < \theta_{FS} < 55°$ with 0.1 mm cubic pillar structures.

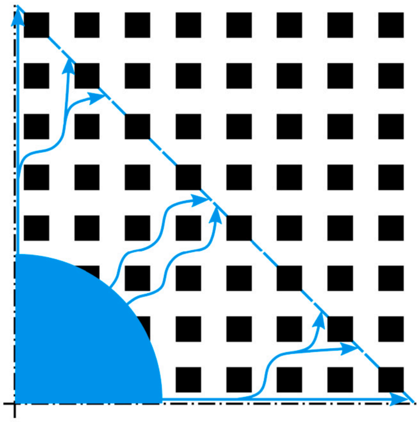

Fig. 6. Schematic representation of flow paths for taxicab distance dominated groove spreading on hydrophilic surfaces.

line originates in the impact point and roughly follows the shape of the gaps between the pillars. Most notably, an almost 90° turn is observed at each intersection for the flow which does not follow a straight groove, indicating that the liquid does in fact follow a close-to-taxicab path, especially in the regions where the highest velocities are still observed.

Once the rapid inertia-driven spreading flow subsides, capillary effects first cause the equilibration of energetically unfavorable spreading shapes: half-filled gaps are filled completely and connect with neighboring grooves, creating a diagonal contact line. This diagonal contact line is a defining feature of the diamond spreading shape. Such diagonal contact lines are experimentally observed in many cases such as the one shown in Fig. 5. In case of hydrophilic, but not superhydrophilic surfaces, the diamond shape remains stable even until the latest stage of spreading.

To compare the overall spreading behavior in the inertial phase, some more general trends can be established from Fig. 8a-b. Here, we show the spreading factor ratios at the end of the inertial phase as determined from the bottom view and simulations, defined as the axial

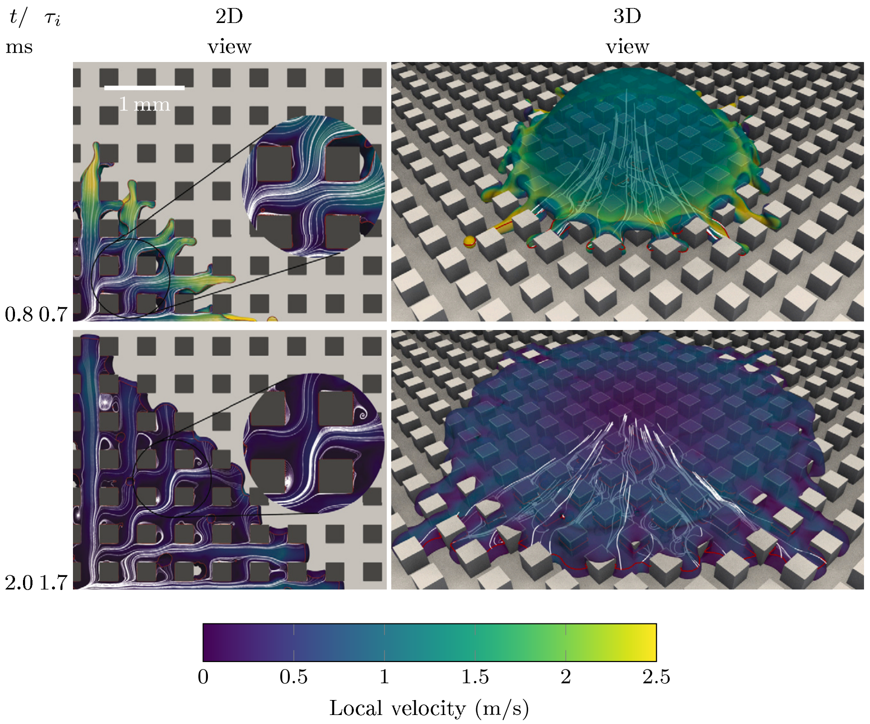

Fig. 7. Comparison of results from Fig. 7 of the main manuscript with experimental data. Droplet impact ($\theta_Y = 10°$ in the simulation) onto untreated $d_s = 0.2$ mm structures. We = 180, Re = 1160.

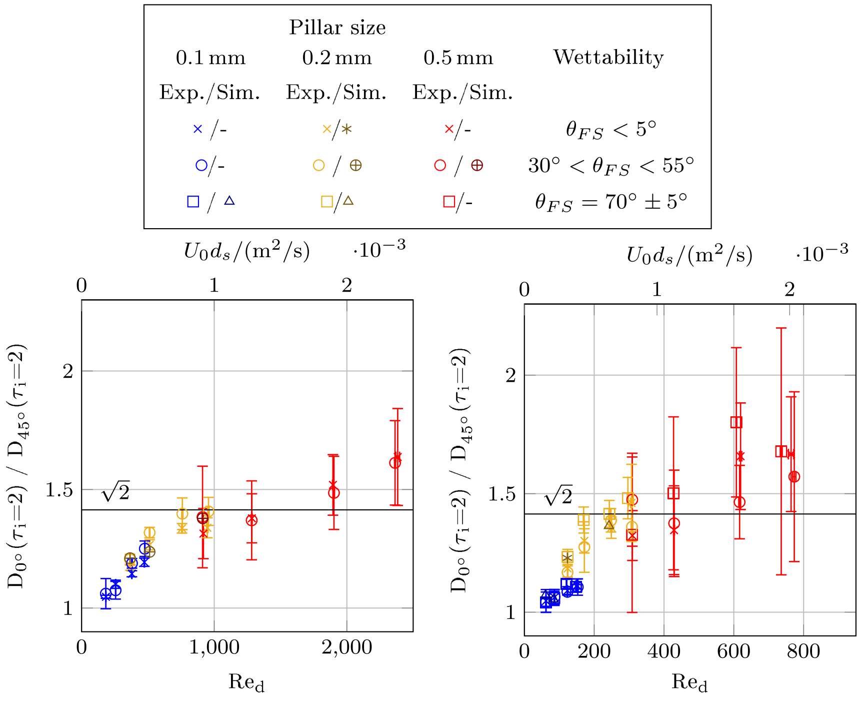

(a) Water

(b) Isopropanol

Fig. 8. Ratio of the spreading factors at the end of the inertial phase ($\tau_i = 2$) for hydrophilic cases $\theta_{FS} \leq 70°$ over the structure-size specific Reynolds number Re_d and the dimensional parameter $U_0 d_s$. Error bars represent standard deviation between 4-6 repetitions and two orthogonal axes (8-12 data points) for each parameter combination.

spreading factor on the y-axis (as defined in Fig. 2) divided by the diagonal spreading factor.

Note that for the results obtained from the simulation, the axial results along the x-axis are omitted here. The symmetry of the impact position along a groove can create an excessive jet along the x-axis. Under experimental conditions, the impact position is never perfectly centered within the groove. As such, if such a jet is formed in experiments in which the impact point is near the center of a groove, even a slight offset and inhomogeneities in the surface cause the jet to impinge and stick on a pillar side before $\tau_i = 2$. This deviation is further discussed in the validation of the numerical methods given in supplementary materials B where figure B.3 shows how such a jet can even cause a droplet to detach. Thus, the axial spreading factors from the simulations used for the determination of the ratios here are those determined on the y-axis (Fig. 2).

In all cases, a higher impact velocity, here expressed through the structure-size specific Reynolds number Re_d seems to mainly increase the axial spreading parameters within a single fluid. Notably, it is increased significantly more with higher Re_d than the diagonal spreading factor, which seems to depend on the non-structure specific Reynolds or Weber number. This causes the spreading factor ratio to increase for higher Re_d. A spreading factor ratio near 1 could indicate top-dominated or top-driven spreading, whereas a spreading factor ratio closer to $\sqrt{2}$ (black line in Fig. 8b) indicates diamond spreading through many flow-splitting intersections. A spreading factor ratio much larger than that indicates jet-dominated spreading. Between both fluids, the diamond spreading condition ($D_{0°}/D_{45°} \approx \sqrt{2}$) is reached at a much smaller Re_d for isopropanol than for water and both behaviors are more comparable in terms of the quantity $\mathrm{Re}_d \mu/\rho = U_0 d_s$, which is shown as a second axis in Fig. 8, as long as the overall spreading process is groove-dominated ($d_s \leq 0.2\,\mathrm{mm}$ for our experiments). This could indicate that Re_d (and thus liquid viscosity) mainly affects whether top-driven or groove-dominated spreading is established, but the shape of the spreading region is dominated by the redirection losses. In the future, extensive parameter variations could clarify the influence of viscosity on the taxicab spreading process. After the formation of the diamond spreading shape (or any other shape), note that in the case of superhydrophilic surfaces, capillary spreading can occur as described by Courbin et al. [8] which affects the final spreading shape and size.

4. Conclusions and outlook

In this work, we have shown how wetted regions in droplet impacts onto structured surfaces form in circular, diamond-like or sharp-tipped shapes. The interplay between inherent wettability, structure size and the impact parameters in determining the spreading shapes in the inertial phase was emphasized. While previous research has emphasized the role of the structure geometry and the capillary spreading phase [8,12,51] we show that wetting of structured surfaces can depend heavily on the impact parameters and the characteristic size of the structures. This can have major implications on the design of surfaces used for spray cooling applications [52], rain and energy harvesting or coating processes. Additionally, while the diamond shapes reported in this study have previously been observed in experiments and simulations [9,26], we give a detailed explanation of the formation of these shapes:

The shape generated by inertial spreading on a surface with sub-millimeter structures is dependent on whether the spreading process is top-driven or groove-driven. For groove-driven flow, the fluid can either follow a single groove as a jet or split up at groove intersections. Low local Reynolds numbers and contact angles promote flow splitting at intersections. If flow-splitting is prevalent in a groove-dominated droplet impact, a diamond shape develops, as the spreading distance is dominated by the taxicab distance in the groove grid. The axial spreading factor is increased significantly more than the diagonal spreading factor for higher impact velocities, as a higher impact velocity promotes a transition from near-circular top-driven spreading to diamond-shaped groove-driven spreading and (at higher values) also causes a transition from diamond-shaped spreading to jetting.

In a future study, the viscosity of the liquids could be varied independently of the surface tension and wettability to accurately determine the influence of viscosity on establishing top-driven spreading and in diamond spreading. Future work is also needed to discuss the effects of the pillar size, wettability and impact conditions on the later capillary spreading phase which happens after the impact inertia has been dissipated and how the shapes attained in the inertial phase influence the final outcome for a variety of conditions. Additionally, the entrapped air bubbles appear to have an effect on the spreading process and their formation, coalescence and disappearance could be discussed in the future.

CRediT authorship contribution statement

Patrick Palmetshofer: Writing – review & editing, Writing – original draft, Visualization, Software, Methodology, Investigation, Formal analysis, Data curation, Conceptualization. **Jonathan Wurst:** Writing – review & editing, Writing – original draft, Visualization, Validation, Software, Methodology, Investigation, Formal analysis, Data curation. **Anne K. Geppert:** Writing – review & editing, Methodology, Conceptualization. **Kathrin Schulte:** Writing – review & editing, Supervision, Software, Project administration, Methodology, Funding acquisition. **Gianpietro Elvio Cossali:** Writing – review & editing, Supervision, Project administration, Methodology, Funding acquisition, Formal analysis, Conceptualization. **Bernhard Weigand:** Writing – review & editing, Supervision, Project administration, Methodology, Funding acquisition, Conceptualization.

Declaration of competing interest

The authors declare that they have no known competing financial interests or personal relationships that could have appeared to influence the work reported in this paper.

Acknowledgements

We appreciate the financial support of this work by the Deutsche Forschungsgemeinschaft (DFG) in the framework of the International Research Training Group “Droplet Interaction Technologies” (GRK 2160/2: DROPIT) under project number 270852890. In addition, we kindly acknowledge funding by the DFG under Germany’s Excellence Strategy - EXC 2075 - 39074001. Furthermore, we appreciate the financial support by the Friedrich and Elisabeth Boysen Foundation under grant “BOY-160”. Lastly, we would like to thank the High-Performance Computing Center Stuttgart (HLRS) for providing computation time on the HPE Apollo Hawk platform under grant number FS3D/11142.

Appendix A. Supplementary material

Supplementary material related to this article can be found online at https://doi.org/10.1016/j.jcis.2024.11.154.

Data availability

Selected simulation and experimental data supporting the findings of this study are available at https://doi.org/10.18419/darus-4178. Additional data are available from the authors upon request (P.P. for experimental data, J.W. for simulation data).

References

[1] J. Kim, Spray cooling heat transfer: the state of the art, Int. J. Heat Fluid Flow 28 (2007) 753–767, https://doi.org/10.1016/j.ijheatfluidflow.2006.09.003.

[2] W. Deng, A. Gomez, Electrospray cooling for microelectronics, Int. J. Heat Mass Transf. 54 (2011) 2270–2275, https://doi.org/10.1016/j.ijheatmasstransfer.2011.02.038.

[3] W.M. Grissom, F. Wierum, Liquid spray cooling of a heated surface, Int. J. Heat Mass Transf. 24 (1981) 261–271, https://doi.org/10.1016/0017-9310(81)90034-x.

[4] C. Neinhuis, W. Barthlott, Characterization and distribution of water-repellent, self-cleaning plant surfaces, Ann. Bot. 79 (1997) 667–677, https://doi.org/10.1006/anbo.1997.0400.

[5] R. Blossey, Self-cleaning surfaces — virtual realities, Nat. Mater. 2 (2003) 301–306, https://doi.org/10.1038/nmat856.

[6] Z. Wang, J.-M. Pereira, E. Sauret, Y. Gan, Emergence of unstable invasion during imbibition in regular porous media, J. Fluid Mech. 941 (2022), https://doi.org/10.1017/jfm.2022.336.

[7] D. Quéré, Non-sticking drops, Rep. Prog. Phys. 68 (2005) 2495–2532, https://doi.org/10.1088/0034-4885/68/11/r01.
[8] L. Courbin, E. Denieul, E. Dressaire, M. Roper, A. Ajdari, H.A. Stone, Imbibition by polygonal spreading on microdecorated surfaces, Nat. Mater. 6 (2007) 661–664, https://doi.org/10.1038/nmat1978.
[9] D. Sivakumar, K. Katagiri, T. Sato, H. Nishiyama, Spreading behavior of an impacting drop on a structured rough surface, Phys. Fluids 17 (2005), https://doi.org/10.1063/1.2033627.
[10] W. Ren, P. Foltyn, A. Geppert, B. Weigand, Air entrapment and bubble formation during droplet impact onto a single cubic pillar, Sci. Rep. 11 (2021), https://doi.org/10.1038/s41598-021-97376-3.
[11] X. Zhou, H. Wang, Q. Zhang, Y. Tian, Q. Deng, X. Zhu, Y. Ding, R. Chen, Q. Liao, Droplet impact on sparse hydrophobic pillar surface: impact phenomena, spreading mode, and droplet breakup, Phys. Fluids 34 (2022) 112101, https://doi.org/10.1063/5.0111786.
[12] X. Li, L. Mao, X. Ma, Dynamic behavior of water droplet impact on microtextured surfaces: the effect of geometrical parameters on anisotropic wetting and the maximum spreading diameter, Langmuir 29 (2013) 1129–1138, https://doi.org/10.1021/la304567s.
[13] H.J. Park, S. Yamagishi, S. Osuka, Y. Tasaka, Y. Murai, Development of multi-cycle rainbow particle tracking velocimetry improved by particle defocusing technique and an example of its application on twisted Savonius turbine, Exp. Fluids 62 (2021), https://doi.org/10.1007/s00348-021-03179-7.
[14] T.-V. Nguyen, M. Ichiki, Bubble entrapment during the recoil of an impacting droplet, Microsyst. Nanoeng. 6 (2020), https://doi.org/10.1038/s41378-020-0158-y.
[15] V. Vaikuntanathan, D. Sivakumar, Transition from Cassie to impaled state during drop impact on groove-textured solid surfaces, Soft Matter 10 (2014) 2991–3002, https://doi.org/10.1039/C4SM00050A, https://pubs.rsc.org/en/content/articlelanding/2014/sm/c4sm00050a.
[16] S. Robson, G.R. Willmott, Asymmetries in the spread of drops impacting on hydrophobic micropillar arrays, Soft Matter 12 (2016) 4853–4865, https://doi.org/10.1039/c5sm03108g.
[17] D. Bartolo, F. Bouamrirene, E. Verneuil, A. Buguin, P. Silberzan, S. Moulinet, Bouncing or sticky droplets: impalement transitions on superhydrophobic micropatterned surfaces, Europhys. Lett. 74 (2006) 299, https://doi.org/10.1209/epl/i2005-10522-3, https://iopscience.iop.org/article/10.1209/epl/i2005-10522-3/meta.
[18] Z. Hu, X. Wu, F. Chu, X. Zhang, Z. Yuan, Off-centered droplet impact on single-ridge superhydrophobic surfaces, Exp. Therm. Fluid Sci. 120 (2021) 110245, https://doi.org/10.1016/j.expthermflusci.2020.110245, https://www.sciencedirect.com/science/article/pii/S0894177720307494.
[19] C. Ishino, K. Okumura, Wetting transitions on textured hydrophilic surfaces, Eur. Phys. J. E 25 (2008) 415–424, https://doi.org/10.1140/epje/i2007-10308-y.
[20] D.I. Yu, S.W. Doh, H.J. Kwak, H.C. Kang, H.S. Ahn, H.S. Park, M. Kiyofumi, M.H. Kim, Wetting state on hydrophilic and hydrophobic micro-textured surfaces: thermodynamic analysis and X-ray visualization, Appl. Phys. Lett. 106 (2015) 171602, https://doi.org/10.1063/1.4919136.
[21] X. Zhang, A. Du, Y. Luo, C. Lv, Y.S. Zhang, S. Yan, Y. Wu, J. Qiu, Y. He, L. Wang, Q. Li, Wetting behaviors and mechanism of micro droplets on hydrophilic micropillar-structured surfaces, Surf. Interf. 33 (2022) 102242, https://doi.org/10.1016/j.surfin.2022.102242, https://www.sciencedirect.com/science/article/pii/S2468023022005077.
[22] L. Xia, Z. Yang, F. Chen, T. Liu, Y. Tian, D. Zhang, Droplet impacting on pillared hydrophobic surfaces with different solid fractions, J. Colloid Interface Sci. 658 (2024) 61–73, https://doi.org/10.1016/j.jcis.2023.12.053.
[23] Y. Song, Q. Wang, Y.Y. Ying, Z. You, S. Wang, J. Chun, X. Ma, R. Wen, Droplet spreading characteristics on ultra-slippery solid hydrophilic surfaces with ultra-low contact angle hysteresis, Coatings (2022), https://doi.org/10.3390/coatings12060755.
[24] P. Foltyn, D. Ribeiro, A. Silva, G. Lamanna, B. Weigand, Influence of wetting behavior on the morphology of droplet impacts onto dry-patterned micro-structured surfaces, Phys. Fluids 34 (2022) 123322, https://doi.org/10.1063/5.0124692.
[25] V. Vaikuntanathan, D. Sivakumar, Maximum spreading of liquid drops impacting on groove-textured surfaces: effect of surface texture, https://doi.org/10.1021/acs.langmuir.5b04639, 2016.
[26] H. Tan, Numerical study on splashing of high-speed microdroplet impact on dry microstructured surfaces, Comput. Fluids 154 (2017) 142–166, https://doi.org/10.1016/j.compfluid.2017.05.014.
[27] K. Eisenschmidt, M. Ertl, H. Gomaa, C. Kieffer-Roth, C. Meister, P. Rauschenberger, M. Reitzle, K. Schlottke, B. Weigand, Direct numerical simulations for multiphase flows: an overview of the multiphase code FS3D, Appl. Math. Comput. 272 (2016) 508–517, https://doi.org/10.1016/j.amc.2015.05.095.
[28] M. Hermans, Selective, laser-induced etching of fused silica at high scan-speeds using KOH, J. Laser Micro Nanoeng. 9 (2014) 126–131, https://doi.org/10.2961/jlmn.2014.02.0009.
[29] R. Tadmor, Line energy and the relation between advancing, receding, and young contact angles, Langmuir 20 (2004) 7659–7664, https://doi.org/10.1021/la049410h.
[30] P. Foltyn, Droplet collisions with dry solid surfaces with variable wettability and topography, Ph.D. thesis, University of Stuttgart, 2022.
[31] IAPWS, Revised release on surface tension of ordinary water substance, Technical Report R1-76, 2014.
[32] J.R. Rumble, Surface Tension at Various Temperatures, CRC Press, Taylor & Francis Group, 2019.
[33] M.L. Huber, R.A. Perkins, A. Laesecke, D.G. Friend, J.V. Sengers, M.J. Assael, I.N. Metaxa, E. Vogel, R. Mareš, K. Miyagawa, New international formulation for the viscosity of H2O, J. Phys. Chem. Ref. Data 38 (2009) 101–125, https://doi.org/10.1063/1.3088050.
[34] J.R. Rumble, Viscosity of Liquids as a Function of Temperature, CRC Press, Taylor & Francis Group, 2019.
[35] W. Wagner, A. Pruß, The IAPWS formulation 1995 for the thermodynamic properties of ordinary water substance for general and scientific use, J. Phys. Chem. Ref. Data 31 (2002) 387–535, https://doi.org/10.1063/1.1461829.
[36] J.R. Rumble, Density rho at the temperature in °C indicated by superscript, CRC Press, Taylor & Francis Group, 2019.
[37] P. Foltyn, D. Ribeiro, A. Silva, G. Lamanna, B. Weigand, Influence of wetting behavior on the morphology of droplet impacts onto dry smooth surfaces, Phys. Fluids 33 (2021) 063305, https://doi.org/10.1063/5.0053539.
[38] C. Hirt, B. Nichols, Volume of fluid (vof) method for the dynamics of free boundaries, J. Comput. Phys. 39 (1981) 201–225, https://doi.org/10.1016/0021-9991(81)90145-5.
[39] W. Rider, D. Kothe, Reconstructing volume tracking, J. Comput. Phys. 141 (1998) 112–152, https://doi.org/10.1006/jcph.1998.5906.
[40] B. Lafaurie, C. Nardone, R. Scardovelli, S. Zaleski, G. Zanetti, Modelling merging and fragmentation in multiphase flows with SURFER, J. Comput. Phys. 113 (1994) 134–147, https://doi.org/10.1006/jcph.1994.1123.
[41] J. Steigerwald, M. Ibach, A.K. Geppert, B. Weigand, Numerical investigation of drop–film interactions with a thixotropic liquid, J. Non-Newton. Fluid Mech. 329 (2024) 105259, https://doi.org/10.1016/j.jnnfm.2024.105259.
[42] J. Potyka, K. Schulte, C. Planchette, Liquid distribution after head-on separation of two colliding immiscible liquid droplets, Phys. Fluids 35 (2023), https://doi.org/10.1063/5.0168080.
[43] B. Mathieu, Etudes physique, expérimentale et numérique des mécanismes de base intervenant dans les écoulements diphasiques en micro-fluidique, Ph.D. thesis, Université de Provence, 2003.
[44] R.G. Cox, The dynamics of the spreading of liquids on a solid surface. Part 1. Viscous flow, J. Fluid Mech. 168 (1986) 169, https://doi.org/10.1017/s0022112086000332.
[45] C. Josserand, S. Thoroddsen, Drop impact on a solid surface, Annu. Rev. Fluid Mech. 48 (2016) 365–391, https://doi.org/10.1146/annurev-fluid-122414-034401.
[46] A. Yarin, Drop impact dynamics: splashing, spreading, receding, bouncing…, Annu. Rev. Fluid Mech. 38 (2006) 159–192, https://doi.org/10.1146/annurev.fluid.38.050304.092144.
[47] S. Chen, V. Bertola, Jumps, somersaults, and symmetry breaking in Leidenfrost drops, Phys. Rev. E 94 (2016) 021102, https://doi.org/10.1103/PhysRevE.94.021102.
[48] W. Ren, J. Reutzsch, B. Weigand, Direct numerical simulation of water droplets in turbulent flow, Fluids 5 (2020) 158, https://doi.org/10.3390/fluids5030158.
[49] M. Broom, G.R. Willmott, Water drop impacts on regular micropillar arrays: the impact region, Phys. Fluids 34 (2022) 017115, https://doi.org/10.1063/5.0078792.
[50] S. Wildeman, C.W. Visser, C. Sun, D. Lohse, On the spreading of impacting drops, J. Fluid Mech. 805 (2016) 636–655, https://doi.org/10.1017/jfm.2016.584.
[51] C.W. Extrand, S.I. Moon, P. Hall, D. Schmidt, Superwetting of structured surfaces, Langmuir 23 (2007) 8882–8890, https://doi.org/10.1021/la700816n.
[52] M. Jiang, Y. Wang, F. Liu, H. Du, Y. Li, H. Zhang, S. To, S. Wang, C. Pan, J. Yu, D. Quéré, Z. Wang, Inhibiting the Leidenfrost effect above 1,000 °C for sustained thermal cooling, Nature 601 (2022) 568–572, https://doi.org/10.1038/s41586-021-04307-3, https://www.nature.com/articles/s41586-021-04307-3.